Multilayer control of an optical reference cavity for space applications

Multilayer control of an optical reference cavity for space applications

José Ospina, *Member, IEEE*, Enrico Canuto, *Senior Member, IEEE,* Andres Molano Jimenez, *Student Member, IEEE,* and Wilber Acuña-Bravo, *Student Member, IEEE*

***Abstract*—The paper deals with multilayer and fine thermal control of an optical reference cavity for space applications. The cavity, made of Ultra Low Expansion glass (ULE), must be kept close to the zero-expansion temperature of the glass (near room temperature). The target can only be met by active control, while leaving the cavity free of sensors and actuators. This is achieved by applying two concepts: thermal bath and reference thermal sink, the latter allowing zero-expansion temperature to be reached by heaters in a wide range of the environment. Guidelines for cavity design and thermal control implementation are detailed together with preliminary experimental results.**

***Index Terms* - Digital control, temperature control, temperature measurement, reference cavity.**

I. INTRODUCTION

FUTURE ESA (European Space Agency) scientific space missions such as LISA (Laser Interferometer Space Antenna) and its precursor [1], DARWIN [2], gravimetric satellite-to-satellite interferometers [3], among others, require laser interferometry as driving technology. In essence, a frequency-stable light radiation is employed as a dimensional standard for very accurate distance measurement/control. To this end, the frequency $f = c/\lambda$ of the light radiation emitted by a monolithic laser source, typically Nd-YAG (Neodimium in Yttrium Aluminum garnet), need be stabilized better than one part in 10^{12} against a frequency standard. The latter may be provided either by atomic/molecular absorption lines or by Fabry-Pérot cavities. Cavities should be preferred in space.

A cavity of this kind [4], [5], [6] is made of a pair of highly reflecting low-loss, spherical mirrors, inserted at the extremes of a hollow cylinder made of low thermal expansion material, for instance glass ceramics like ULE, having a coefficient of thermal expansion (CTE) which is lower than $3\times10^{-8}\ \mathrm{K}^{-1}$ around room temperature ($\theta \cong 20\ ^\circ\mathrm{C}$), and crosses zero at some specific temperature $\underline{\theta}$, referred to as the zero-expansion temperature (ZET). To achieve dimensional stability in the order of 10^{-12}, (i) thermal instability must be better than $0.1\ \mathrm{mK}$ at room temperature, having assumed that ZET can be calibrated better than $1\ \mathrm{K}$, (ii) cavity mounting and environment must guarantee that the only sensible cause of deformation is of thermo-elastic nature in the frequency band of interest, which is below 1 Hz for the space missions addressed in [1], [2] and [3], (iii) the optical path of the laser beam between mirror reflecting surfaces must be independent of the environment (uniform and stable index of refraction). In space, only the first condition is stringent, the others being naturally achieved except for the second one during launch, so as not to damage and stress the cavity.

A. Literature and paper outline

Fabry-Pérot cavities made of low expansion glass and thermally stabilized below $0.1\ \mathrm{mK}$ at room temperature have been employed by National Institutes of Standards as reference standards capable of guaranteeing fractional frequency stabilities well below 10^{-12} over several hours [4], [5], and [6]. Sub-millikelvin thermal stabilization of the cavity is usually obtained by mixed passive/active means: the cavity is thermally insulated by vacuum and supports, which latter must also damp vibrations. The metal walls of the vacuum chamber are thermally stabilized at room temperature better than 10 mK by an active control system. The vacuum chamber is then thermally insulated from the surrounding air, except for windows transmitting the laser beam.

Cavity thermal equilibrium and stability can be reached without active thermal control. Passive stabilization may be

Manuscript received September 29, 2007. Accepted for publication March 23, 2010. This work was supported in part by Regione Piemonte research project E2 "Riferimenti ultrastabili di frequenza ottica per interferometria laser in applicazioni spaziali (RUFO, Ultra stable optical references for space laser interferometry)".

José Ospina is with Politecnico di Torino, Dipartimento di Automatica e Informatica, Corso Duca degli Abruzzi 24, 10129 Torino, Italy (e-mail: jose.ospina@polito.it).

Enrico Canuto is with Politecnico di Torino, Dipartimento di Automatica e Informatica, Corso Duca degli Abruzzi 24, 10129 Torino, Italy (phone: +39 011 564 7026; fax: +39 011 564 7198; e-mail: enrico.canuto@ polito.it).

Andres Molano Jimenez is with Politecnico di Torino, Dipartimento di Automatica e Informatica, Corso Duca degli Abruzzi 24, 10129 Torino, Italy (e-mail: andres.molanojimenez@polito.it).

Wilber Acuña-Bravo is with Politecnico di Torino, Dipartimento di Automatica e Informatica, Corso Duca degli Abruzzi 24, 10129 Torino, Italy (e-mail: wilber.acunabravo@polito.it).

favored by the cavity size, especially thickness, ensuring very large time constants (>10h) of the in-vacuum cavity-chamber irradiation. For instance, the on-ground prototype of the LISA optical reference [7] claims thermal stability inside the shields of the order of $\mu K/\sqrt{Hz}$. Passive stabilization looks appealing owing to some difficulties in employing thermal actuators and sensors.

1) Sensor electronics is a source of drift and noise at the measurement point, which implies sensors not to be located on the cavity but on a thermal shield so as to filter drifts.
2) Thermo-electric coolers (TEC) would impose either thermal connections between cavity and chamber or complex radiators, thus increasing the risk of mechanical/acoustical vibrations.
3) Thermal blankets (wound heaters) look a simpler solution, but they require either ZET is set higher than the environment, or a two-layer thermal control is implemented for transferring internal heat to environment.

On the contrary, active cavities can be made smaller than passive ones, are suitable to different conditions, can be mounted separately from the payload, monitored and commanded from the ground. These properties look appealing for space applications, which require cavity and supporting structure to withstand launch loads. This study aims to verify under which conditions active thermal control can perform like passive control. Advantages of active control encompass well defined and selectable set-points, programmable transient to set-point and repeatable stabilization performance.

Active temperature control is essential in material [8], industrial [9], [10], [12] and domestic processes [13]. The generic control goal is to ensure that measured temperatures smoothly reach and track (variable) set points notwithstanding unpredictable user actions [13], nonlinearities in heat transfer, uncertainty of model parameters [8], unavoidable thermal runaways and drifts [8], process time variability, cross-couplings [10] and time delays [12]. Temperature actuator/sensor selection and location is always a major problem as in [11] and [13], because of the distributed and multivariate nature of thermal processes. Control design varies from the classical Bode design of linearized models with stability analysis versus parameter uncertainty [8], adaptive and decoupled model predictive technique [10], fuzzy control [12], and neural networks [14], [15]. Here state-equation modeling and design are afforded within the framework of Embedded Model Control (see [16] for an outline of the theory and [17], [18] and [19] for applications).

First, geometry, materials and principles of two cavities are reported: (i) a preliminary cavity exists but clamping suspensions prevents target frequency stabilization; (ii) suspension and thermal control re-design lead to an improved cavity, named RUFO from the acronym of the sponsoring research project (Section B). Requirements driving cavity design and thermal stabilization are presented in Section II. Cavity thermodynamics is then outlined, leading to a pair of simple lumped-parameter dynamics (Section III). Converting continuous-time dynamics to discrete time leads to five embedded models that are part of the control unit outlined in Section IV. Implementation of the thermal control system is afforded in Section V: design guidelines for sensors and actuators are treated. Section VI is devoted to some experimental results on a preliminary cavity regulated by a wound heater, and on the thermo-electric control of a plate emulating a reference sink. Experimental results lead to the RUFO cavity design.

B. Geometry, materials and concepts

A pair of cavities have been implemented.

1) Preliminary cavity. An existing, cylindrical cavity made by ULE is clamped at both extremes using pre-loaded cup flexures in Vespel. The latter are inserted into radial supports in aluminum. The exploded 3D view is shown in Fig. 1.

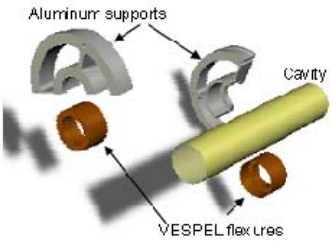

Fig. 1 Exploded view of the preliminary cavity.

2) RUFO cavity (Fig. 2).

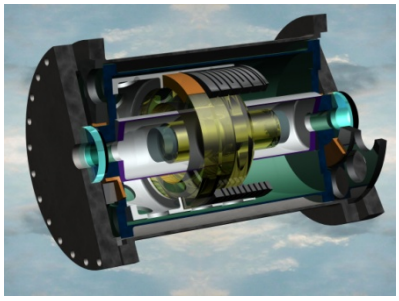

Fig. 2 Artist's impression of the RUFO cavity.

A new cavity has been designed (i) to be small and compact, less than 250×150 mm (length×diameter), (ii) to withstand launch loads, and (iii) to be thermally regulated. The essential concepts are: (i) freedom of a longitudinal deformation, which has been solved by a single cylindrical glass monolith shaped as a cup and carrying axially the optical cavity, (ii) separation of the supporting interface: the cup, not the cavity, will be pre-loaded by means of a suitable flexure so as to withstand launch loads, (iii) thermal bath concept: commanded heaters generate uniform radiating surfaces surrounding the cavity at the ZET, (iv) reference sink

concept: the cavity thermal bath and the environment are thermally separated, thus allowing the cavity ZET to be any within the range $\Delta\underline{\theta} = \pm 15$ K, suggested by manufacturer. The sink concept is implemented through multi-layer radiating surfaces, called inner and outer cavity shields, and insulating connections between cup, shields and chamber. The ensemble is under commissioning. A dummy cavity for testing control electronics and code is also available, having replaced ULE cavity with a Plexiglas one.

II. Stability Requirements

A. Frequency stability

For the space applications [1], [2] and [3], frequency instability, averaged over short periods $\tau_0 \geq 1$ s, must be less than 1 part in 10^{12} during time periods longer than $\tau_1 \geq 10^4$ s. Frequency instability cannot be assumed to be a long-term stationary process because of electronics noise entering the optical reference control loop. To this end, the bound to fractional frequency instability $\partial\nu(t)$ is expressed by combining white and (non-stationary) flicker noise. By limiting the analysis to finite-time periods, instability realizations become part of longer term stationary processes and therefore spectral density can be defined, though drifting toward lower frequencies. Denote the root of the unilateral spectral density (PSD for short) of $\partial\nu(t)$ with $S_\nu(f)$, being restricted to the measurement bandwidth (MBW) of interest, i.e. to

$$\mathcal{F} = \left\{ f_1 = \tau_1^{-1} \leq f \leq f_0 = \tau_0^{-1} \right\}. \tag{1}$$

The spectral bound $\bar{S}_\nu(f)$ is defined as

$$\begin{aligned} &\bar{S}_\nu^2(f) = \bar{S}_0^2 + \bar{S}_{-1}^2 / f \\ &\sqrt{\int_{f_1}^{f_0} \bar{S}_\nu^2(f)\,df} \leq \bar{\sigma}_\nu = 10^{-12}. \end{aligned} \tag{2}$$

Frequency stability requirement in (2) is converted into thermal stability conditions in the following section, by exploiting ULE thermal expansion around the ZET $\underline{\theta}$.

B. Thermal stability

Thermal stability requirements are obtained from the Fabry-Pérot differential equation [18], and by restricting to longitudinal deformation. Start from the Fabry-Pérot cavity differential equation around a resonance pair (optical frequency, cavity length)$=(\nu_0, L_0)$ defined by

$$\nu_0 L_0 = Nc/2,\ N \text{ integer}, \tag{3}$$

where c is the speed of light in vacuum, ν_0 is the frequency of the injected laser beam, and L_0 the length of the optical path between the beam spot centers on the cavity reflecting mirrors. Denoting time-varying frequency and length detuning with $\Delta\nu(t)$ and $\Delta L(t)$, the following equation results

$$\nu_0^{-1}\Delta\nu(t) = \partial\nu(t) = L_0^{-1}\Delta L(t) + \varepsilon(t) = \partial L(t) + \varepsilon(t), \tag{4}$$

less a fractional residual error ε. The left-hand side term and the first term in the right-hand side are referred to as frequency and length (fractional) instability, respectively, not to be confused with 'closed-loop' instability, applicable to control systems.

Only instability due to thermal effects is considered. Denote the thermal gradient with $\Delta\theta(x,t) = \underline{\theta} - \theta(x,t)$, where $\underline{\theta}$ depends on the glass CTE properties. The cavity temperature must be moved and kept close to $\underline{\theta}$ for the entire mission. The coordinate x is the longitudinal cavity dimension along the light path from $-L_0/2$ to $L_0/2$, which must be kept unaffected by thermal deformations. The cavity centre corresponds to $x = 0$. The longitudinal cavity temperature profile is decomposed into the sum of two 2nd order Legendre polynomials in the variable x: the first has coefficients $\lambda = \{\lambda_0, \lambda_1, \lambda_2\}$ which are independent of time and represent the steady-state profile error; the second one has coefficients $\delta(t) = \{\delta_0(t), \delta_1(t), \delta_2(t)\}$, which account for time fluctuations due to control jitter and residual disturbance effects.

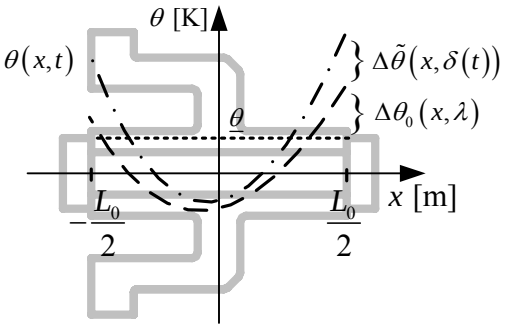

Fig. 3 Cavity temperature profile decomposition.

The general form of a 2nd order Legendre polynomial is

$$\Delta\theta(x,\alpha) = \alpha_0 + \alpha_1(2x/\underline{L}) + \frac{1}{2}\alpha_2\left((2x/\underline{L})^2 - \frac{1}{3}\right). \tag{5}$$

Coefficients in (5) may be obtained from temperature values at three selected points, like $\Delta\theta(-L/2)$, $\Delta\theta(0)$ and $\Delta\theta(L/2)$. Solving (5) for α provides the equation

$$\begin{bmatrix} \alpha_0(t) \\ \alpha_1(t) \\ \alpha_2(t) \end{bmatrix} = \begin{bmatrix} 1/6 & 2/3 & 1/6 \\ -1/2 & 0 & 1/2 \\ 1 & -2 & 1 \end{bmatrix} \begin{bmatrix} \Delta\theta(-L/2,t) \\ \Delta\theta(0,t) \\ \Delta\theta(L/2,t) \end{bmatrix}. \tag{6}$$

The whole cavity temperature profile (see Fig. 3) is then written as

$$\theta(x,t) = \underline{\theta} + \Delta\theta_0(x,\lambda) + \Delta\tilde{\theta}(x,\delta(t)), \tag{7}$$

where both $\Delta\tilde{\theta}(x,\delta(t))$ and $\Delta\theta_0(x,\lambda)$ are Legendre polynomials with coefficients λ and $\delta(t)$, respectively.

ULE manufacturer's data suggest that CTE can be expressed, around room temperature, as a 1st order polynomial

$$CTE(\theta(t)) = \beta(\theta(t) - \underline{\theta}), \tag{8}$$

with $\beta = 2\times10^{-9}$. Cavity longitudinal expansion is obtained integrating temperature variations times the CTE, that is, as

$$\partial L(t)=\frac{\Delta L}{\underline{L}}=\frac{1}{2}\int_{-\underline{L}/2}^{\underline{L}/2}\beta\left(\theta(x,t)-\underline{\theta}\right)^2 dx\,, \tag{9}$$

where $\underline{L}$ is the cavity length at ZET $\underline{\theta}$. By replacing (7) in (9), cavity length instability becomes the sum of a steady and a variable term, $\partial L(t)=\partial L_0+\partial\tilde{L}(t)$, with the time varying component holding

$$\partial\tilde{L}(t)=\beta(\delta_0^2(t)+\frac{\delta_1^2(t)}{3}+\frac{\delta_2^2(t)}{45}+2\delta_0(t)\lambda_0+ +\frac{2\delta_1(t)\lambda_1}{3}+\frac{2\delta_2(t)\lambda_2}{45}) \tag{10}$$

Equation (10) shows the variable term of $\partial L(t)$ depends on both steady and variable thermal coefficients λ and $\delta(t)$ in (7). Since the cavity is by construction sensor and actuator free, the most significant sources of $\Delta\theta_0(x,\lambda)$ and of $\Delta\tilde{\theta}(x,\delta(t))$ come from the surrounding bath temperature and from the uncertainty on ZET $\underline{\theta}$. Specifically, bath fluctuations due to control jitter affect $\Delta\tilde{\theta}(x,\delta(t))$ in a pure random way, with a spectral density $S^2_{\Delta\theta}(f)$ which is assumed to be uniform along the cavity. Bath set-point error due to sensor calibration affects $\Delta\theta_0(x,\lambda)$. In practice any temperature $\theta(t,x)$ in (7) may be rewritten as

$$\theta(x,t)=\underline{\theta}+e_s(x)+e_{\underline{\theta}}(x)+e_r(t)\,, \tag{11}$$

where e_s is the set-point error (steady), $e_{\underline{\theta}}$ is the ZET uncertainty (steady) and e_r is a random component. Denoting the largest steady errors with e_{sm} and $e_{\underline{\theta}m}$, and assuming a worst-case profile of them along the cavity, the following bounds on the λ coefficients result from (6):

$$\begin{aligned}\lambda_{0m}&=e_{\underline{\theta}m}+e_{sm}\\ \lambda_{1m}&=e_{sm}\\ \lambda_{2m}&=4e_{sm}\end{aligned}\,. \tag{12}$$

Likewise, equation (6) allows to derive the following spectral density of the δ coefficients:

$$\begin{aligned}S^2_{\delta0}(f)&=1/2\,S^2_{\Delta\theta}(f)\\ S^2_{\delta1}(f)&=1/2\,S^2_{\Delta\theta}(f)\\ S^2_{\delta2}(f)&=6S^2_{\Delta\theta}(f)\end{aligned}\,. \tag{13}$$

By including (13) and (12) in (10) and by neglecting second order terms in δ, the spectral density of the length instability results as

$$S^2_{\Delta L}(f)\simeq 8\beta^2\left(e^2_{sm}+2e_{sm}e_{\underline{\theta}m}+e^2_{\underline{\theta}m}\right)S^2_{\Delta\theta}(f)\,. \tag{14}$$

Applying the bound in (2) to the length instability PSD in (14), a bound to thermal instability results. In the case interchangeable thermistors with uncertainty of 0.1 K are employed for bath regulation, and no ZET calibration is performed, the peak values of the steady errors may be set to $e_{\underline{\theta}m}=\Delta\underline{\theta}=15$ K, and $e_{sm}=0.1$ K, and the thermal instability bound inside the MBW (1) results into

$$S_{\Delta\theta}(f)\le 20\ \mu\text{K}/\sqrt{\text{Hz}}\,. \tag{15}$$

Calibrating the ZET better than $e_{\underline{\theta}m}\le e_{sm}=0.1$ K, a more relaxed bound is obtained, namely

$$S_{\Delta\theta}(f)\le 1.7\ \text{mK}/\sqrt{\text{Hz}}\,. \tag{16}$$

Further relaxation of the thermal bound (16) must pass through differential calibration of the bath sensors.

III. Thermodynamics

Cavity thermodynamics derives from the concepts outlined in Section I.B:

1) thermal bath in vacuum is guaranteed by three thermally regulated shields surrounding the cavity;
2) multilayer thermal regulation is capable of transferring heat from shields to environment through a reference thermal sink consisting of the chamber walls, to be regulated at a suitable set-point by TEC, and radiators.

Fig. 4 shows the simplified block-diagram of the multilayer thermal regulation. Solid lines indicate designed heat transfer; dashed lines parasitic transfer. Three thermal baths are deemed necessary (each including one heated shield and a part of the cavity) because of the complex cavity shape dictated by launch loads. As a baseline, only the chamber walls (left and right) are directly thermally regulated by TEC for simplicity's sake.

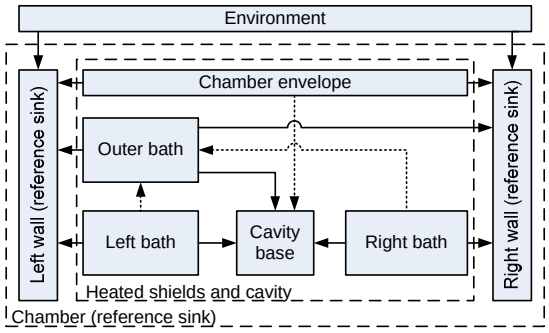

Fig. 4 Simplified block-diagram of the multilayer thermal regulation.

First, time continuous equations are derived, to be later discretized in view of the embedded model. Discretization assumes a control time unit T to be fixed in Section IV.

A. Shields and thermal bath

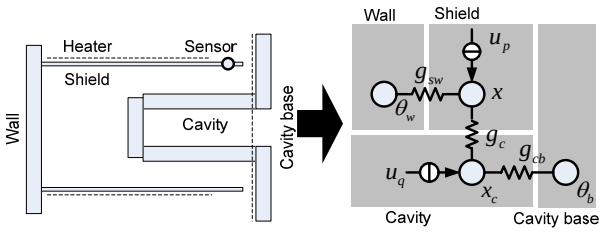

Fig. 5 Layout and equivalent thermal circuit of a single bath.

Each thermal bath in Fig. 4 consists of an aluminum cylinder completely covered by a flexible heater and a temperature sensor mounted on the right extreme of the shield in Fig. 5, i.e. close to the cavity base. Sensor selection

is treated in Section V.A.

The lumped-parameter dynamics in Fig. 5 shows four thermal nodes: (i) two of them, shield and cavity, are given finite thermal capacity, and their internal energy (to be regulated) is proportional to a pair of state variables, x and x_c; the latter denote the mean temperature of shield and cavity, respectively; (ii) wall and cavity-base nodes are assumed infinite capacity, which implies their temperatures, θ_w and θ_b, are variable disturbances.

State equations are written upon definition of the state variable $\Delta x_c = x_c - x$, i.e. the gradient between shield and cavity, and of two input signals $d_{sw}(t) = g_{sw}(\theta_w - x)$ and $d_{cb}(t) = g_{cb}(\theta_b - x_c)$. The latter account for heat exchange from/to ambient. The lumped-parameter model in Fig. 5 results into

$$\begin{aligned}\begin{bmatrix}\dot{x}\\ \Delta\dot{x}_c\end{bmatrix}(t) &= \begin{bmatrix}0 & p_s\\ 0 & -p_c - p_s\end{bmatrix}\begin{bmatrix}x\\ \Delta x_c\end{bmatrix}(t) + \\ &+ \begin{bmatrix}b'_s & 0\\ -b'_s & b_c\end{bmatrix}\begin{bmatrix}u_p\\ u_q\end{bmatrix}(t) + \begin{bmatrix}b'_s & 0\\ -b'_s & b_c\end{bmatrix}\begin{bmatrix}d_{sw}\\ d_{cb}\end{bmatrix}(t)\,. \qquad (17)\\ y(t) &= \begin{bmatrix}1 & 0\end{bmatrix}\begin{bmatrix}x\\ \Delta x_c\end{bmatrix}(t) + e(t) = y_m(t) + e(t)\end{aligned}$$

In (17) $b'_s = 1/C_s$ and $b_c = 1/C_c$ are the inverse of shield and cavity capacities, respectively, $p_s = g_c/C_s$ and $p_s = g_c/C_c$ are thermal poles, u_p denotes the heater power, u_q denotes cavity mirror losses, y is the sensor measure, y_m is the model output and e the model error. The latter variable accounts for measurement error and model discrepancies [16].

Exact discretization of (17) yields

$$\begin{aligned}\begin{bmatrix}x\\ \Delta x_c\end{bmatrix}(i+1) &= \begin{bmatrix}1 & \dfrac{p_s\left(1-e^{-(p_c+p_s)T}\right)}{p_c+p_s}\\ 0 & e^{-(p_c+p_s)T}\end{bmatrix}\begin{bmatrix}x\\ \Delta x_c\end{bmatrix}(i) + \\ &+ B\begin{bmatrix}u_p\\ u_q\end{bmatrix}(i) + G\begin{bmatrix}d_{sw}\\ d_{cb}\end{bmatrix}(i) \qquad ,(18)\\ y(i) &= \begin{bmatrix}1 & 0\end{bmatrix}\begin{bmatrix}x\\ \Delta x_c\end{bmatrix}(i) + e(i)\end{aligned}$$

Details of B in (18) are omitted for brevity's sake. Since $p_c T < 0.001$, equations (18) can be simplified by developing the exponential terms up to the 1st degree entry of the power series, thus leading to

$$\begin{aligned}\begin{bmatrix}x\\ \Delta x_c\end{bmatrix}(i+1) &= \begin{bmatrix}1 & p_s T\\ 0 & 1-(p_s+p_c)T\end{bmatrix}\begin{bmatrix}x\\ \Delta x_c\end{bmatrix}(i) + \\ &+ \begin{bmatrix}b_s & 0\\ -b_s & b_c\end{bmatrix}\begin{bmatrix}u_p\\ u_q\end{bmatrix}(i) + \begin{bmatrix}T & 0\\ -T & T\end{bmatrix}\begin{bmatrix}d_{sw}\\ d_{cb}\end{bmatrix}(i)\end{aligned} \qquad ,(19)$$

with $b_s = T/C_s$ and $b_c = T/C_c$. The output equation in (17) remains the same.

The thermal bath concept first implies the shield temperature x must be regulated around ZET $\underline{\theta}$, leaving the cavity to track x within target fluctuations. Second, the shield-cavity heat exchange $p_s T \Delta x_c$ must be treated as a disturbance to be rejected as it must be done with the shield-to-wall exchange d_{sw} in (17). Since disturbance rejection must passes through measurements, when no direct measurement is possible as in this case, Embedded Model Control [16] suggests to describe disturbances as the output of an observable stochastic dynamics. The latter is driven by a noise vector to be real-time extracted from the shield sensor output y. Experimental measurements and simulation suggested to employ a 2nd order dynamics, driven by three noise components collected in the vector

$$\mathbf{w}(i) = \begin{bmatrix}w_0\\ w_w\\ w_2\end{bmatrix}(i)\,. \qquad (20)$$

The overall shield perturbation, in Kelvin units,

$$d_s(i) = w_0(i) + x_d(i) \qquad (21)$$

is written as a combination of a noise w_0 and a random drift x_d. The overall embedded model, combination of (19) and (21), becomes 3rd order and reads

$$\begin{aligned}\begin{bmatrix}x\\ x_d\\ a\end{bmatrix}(i+1) &= \begin{bmatrix}1 & 1 & 0\\ 0 & 1 & 1\\ 0 & 0 & 1\end{bmatrix}\begin{bmatrix}x\\ x_d\\ a\end{bmatrix}(i) + \begin{bmatrix}b_s\\ 0\\ 0\end{bmatrix}u_p(i) + \begin{bmatrix}w_0\\ w_1\\ w_2\end{bmatrix}(i) \qquad .(22)\\ y_m(i) &= \begin{bmatrix}1 & 0 & 0\end{bmatrix}\begin{bmatrix}x & x_d & a\end{bmatrix}^T(i)\end{aligned}$$

In (22), $a(i)$ is a further state is needed to make disturbance dynamics 2nd order. A single parameter, b_s, must be identified in (22). The relevant block diagram is in Fig. 6, where a boxed Σ represents a discrete-time integrator

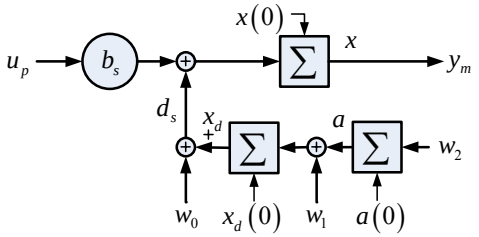

Fig. 6 Embedded model of each shield.

As a final simplification, the embedded models of the three shields are assumed to be decoupled, which means that cross-coupling through the cavity base (Fig. 4) and parasitic heat exchange in Fig. 4 become hidden components of the stochastic disturbance x_d.

B. Reference thermal sinks

To enable shields keeping the cavity bath temperature close to ZET, wherever it lies within ULE manufacturer's range, a reference sink (the chamber in Fig. 4) is built around the bath. The sink is loaded with the chamber thermal capacity and the bath-to-sink positive gradient. It might be loaded also with the thermal bath capacity, should the entire ensemble be cooled with respect to environment. TEC actuators are essential to the purpose. Different layouts

are possible: an easy-to-mount, but not thermally effective, solution has been adopted (see Fig. 7).

Two sets of actuators are located on the opposite walls (left and right) of the chamber; heat is transferred between environment and the TEC hot side through radiators, without any thermal contact with ground. In a more effective layout, TEC hot side should be grounded. Chamber envelope must be properly insulated. TEC design guidelines are treated in Section V.B.

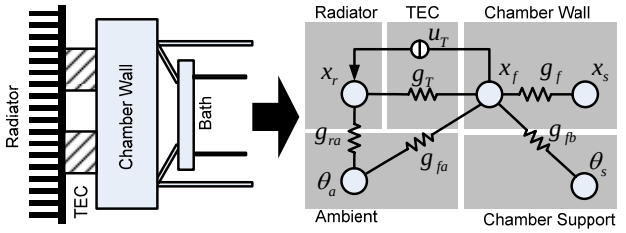

Fig. 7 Layout and equivalent thermal circuit of a single wall (thermal capacities are omitted).

In Fig. 7, TEC units pump heat u_T from chamber wall into a radiator, which in turns conveys it to the environment. Heat sources for the vacuum chamber wall, other than TEC, are dissipation to the environment, heat exchange with thermal bath at temperature θ_s, TEC heat conduction. A further capacity node with state variable x_s, must be included to account for thermal capacity between TEC and sensor, because of wall thickness. In Fig. 7, x_f is the state variable of the left portion of the wall capacity, where TEC units are installed. A single sensor is installed in the right portion of the wall, so as to approach the measurement of x_s. As a result the following 2nd order state equation is written

$$\begin{bmatrix} x_s \\ \Delta x_s \end{bmatrix}(t) = \begin{bmatrix} 0 & p_f \\ 0 & -p_f - p_g \end{bmatrix}\begin{bmatrix} x_s \\ \Delta x_s \end{bmatrix}(t) + \begin{bmatrix} 0 & 0 \\ b_t & 1 \end{bmatrix}\begin{bmatrix} u_T \\ d \end{bmatrix}(t)$$
$$y(t) = \begin{bmatrix} 1 & 0 \end{bmatrix}\begin{bmatrix} x_s \\ \Delta x_s \end{bmatrix}(t) + e(t) \quad . \quad (23)$$

In (23), $\Delta x_s = x_f - x_s$ is the gradient along the chamber wall from TEC unit to sensor, C_f and C_g are the thermal capacities of the left and right wall portions, respectively. The command gain holds $b_t = -sN\underline{\theta}/C_f$, where s denotes the Seebeck coefficient, and N is the number of TEC units. Finally $p_f = g_f/C_f$ and $p_g = g_f/C_g$ are poles accounting for TEC-to-sensor heat conduction.

The disturbance signal d in (23), collecting heat exchange through wall other than TEC thermal flow, satisfies the equation

$$d = g_{fa}\left(\theta_a - x_f\right) + g_{fs}\left(\theta_s - x_f\right) + g_T\left(x_r - x_f\right). \quad (24)$$

Conversion of (23) into discrete-time follows the same approach used in Section A: exponential terms are developed up to 1st degree, and a 2nd order stochastic dynamics accounts for unknown disturbances. The following 4th order state equation results

$$\begin{bmatrix} x_s \\ \Delta x_s \\ x_d \\ a \end{bmatrix}(i+1) = \begin{bmatrix} 1 & 1 & 0 & 0 \\ 0 & 1-\beta & 1 & 0 \\ 0 & 0 & 1 & 1 \\ 0 & 0 & 0 & 1 \end{bmatrix}\begin{bmatrix} x_s \\ \Delta x_s \\ x_d \\ a \end{bmatrix}(i) + \begin{bmatrix} 0 \\ b_t \\ 0 \\ 0 \end{bmatrix}u_T(i) + \mathbf{w}(i) \quad .,(25)$$
$$y_m(i) = \begin{bmatrix} 1 & 0 & 0 & 0 \end{bmatrix}\begin{bmatrix} x_s \\ \Delta x_s \\ x_d \\ a \end{bmatrix}(i)$$

In (25) the following parameters are used

$$\beta = Tg_f\left(C_s^{-1} + C_s^{-1}\right)$$
$$b_t = \beta Ts\underline{\theta}N/\left(C_s + C_f\right), \quad (26)$$

and noise components are

$$\mathbf{w}^T(i) = \begin{bmatrix} w_0 & w_1 & w_2 & w_3 \end{bmatrix}(i). \quad ,(27)$$

The block diagram of (25) is shown in Fig. 8.

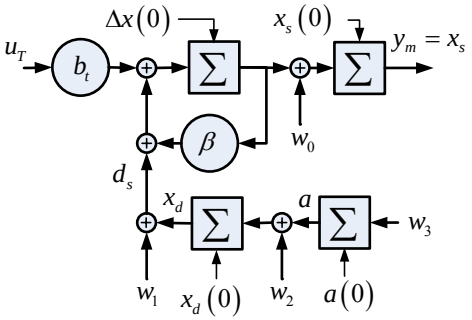

Fig. 8 Embedded model of each chamber wall.

IV. Embedded Model Control

A. Control principles

Bath and reference sink control units may be decoupled, since cross-coupling terms are treated as unknown disturbances. Decoupling does not apply to reference trajectories, as compatible trajectories must be imposed to shields for guaranteeing that cavity reaches the zero-expansion temperature $\underline{\theta}$, and that heater commands do not saturate to zero. Reference trajectory design is not treated here. Moreover, bath set-point should be coordinated with the sink, and the latter should be reached before shield heating. Note, however, coordination might be avoided (full decoupling) leaving bath control to switch off, when shield temperature overshoots $\underline{\theta}$.

Control BW (see Section VI) is limited by heat transport delays and neglected thermistor dynamics, the latter having a cutoff frequency $f_s \cong 0.1$ Hz. Control time unit T is bounded by sensor acquisition electronics, and has been

fixed to Nyquist frequency $f_{\max} \cong f_s$; as a result $T = 3$ s.

As is well known, feedback control cannot eliminate the low-frequency components of the measurement error $e(t)$ in (17) and (23) from the performance variable, i.e. from the actual bath temperature. Moreover, power losses and ambient temperature may produce measurement errors larger than 1 mK, implying thermal control performance strictly depends on sensor design.

B. Digital control implementation

Digital control is based on the Embedded Model Control architecture [16] which consists of embedding (programming) a model of the plant into the control unit and keeping the model state variables up-to-date through plant measurements. This is done, as in Kalman filtering, by a continuous estimation of the noise signal $\mathbf{w}$ in (22) and (25) . Under linear dynamics, the latter is estimated as a linear combination of the model error $e = y - y_m$, where y is the measured temperature of each shield/wall and y_m the output of the corresponding embedded model.

The embedded model provides a prediction of the state variables to be used in computing the next digital command, and a prediction of the disturbance states to be cancelled. To this end, the control law must:

1) drive shield and wall temperatures to track feasible trajectories while respecting restrictions on command bound and slew rate,
2) cancel disturbances,
3) keep the effect of the residual disturbance (mainly noise and prediction errors) bounded.

With reference to (22) and (25), shield control law is written as

$$u_p(i+1) = \underline{u}_p(i+1) + k\left(\underline{x}(i+1) - x(i+1)\right) - x_d(i+1), \quad (28)$$

whereas wall control law becomes

$$\begin{aligned} u_T(i+1) &= \underline{u}_T(i+1) + k_1\left(\underline{x}_s(i+1) - x_s(i+1)\right) + \\ &+ k_2\left(\Delta\underline{x}_s(i+1) - \Delta x_s(i+1)\right) - x_d(i+1) \end{aligned}. \quad (29)$$

In (28) and (29), $\underline{u}_p(i)$ and $u_T(t)$ are nominal commands which would drive the system, in absence of disturbance, along reference trajectories. The latter ones are denoted with $\underline{x}$ (shield), $\underline{x}_s$ (wall) and $\Delta\underline{x}$ (thermal gradient TEC-to-sensor). The term $-x_d(i+1)$ in (28) and (29) cancels the disturbance signals which are updated by the embedded model. In total, only three control gains have to be tuned, namely k in (28) and k_1, k_2 in (29). Commands are properly converted to be digital signals and then dispatched to plant (DAC) and to the embedded models. Care must be exerted in dispatching the same signal, at the same time, to plant and model.

Embedded models, as shown in Fig. 6 and Fig. 8, and in (22) and (25), are discrete-time and rather simple. Therefore, computation at each control step just consists of a few multiplications and additions, allowing the controller to be implemented as a single task. In addition, since embedded models and their variables are directly related to plant thermodynamics, control engineer can access significant variables (disturbance, intermediate state variables) other than commands and measurements.

V. Hardware Architecture and Components

Digital control has been implemented on a National Instruments (NI) PXI controller; it includes additional modules to generate and digitize control signals. Custom electronics has been developed for driving TEC units. The architecture of the overall control unit is sketched in Fig. 9.

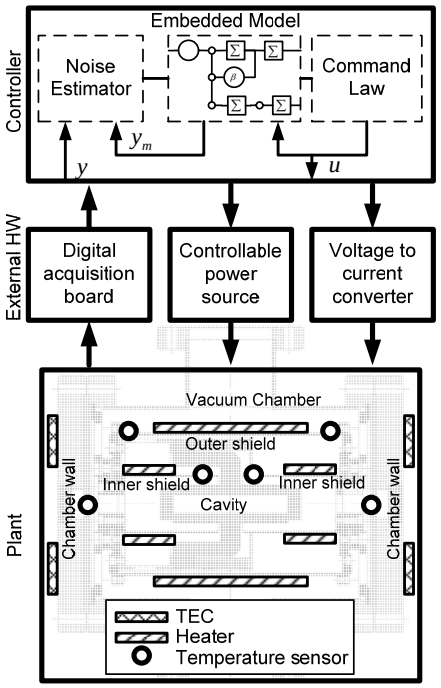

Fig. 9 Hardware architecture.

Concepts in sensor and actuator design as well as their characteristics are briefly outlined below.

A. Sensor selection and design

Temperature measurement supplies the temperature of the sensor substrate θ, which is different from the shield temperature x. Any difference between x and θ enters the temperature measurement error $e = x - \theta$ defined in Section II.B. Factors causing θ to differ from x are here described through a static thermal model as in Fig. 10, which assumes the following elements and interactions.

1) Thermal nodes are i) the shield temperature x, ii) the sensor substrate temperature θ, iii) the wire temperature θ_f, iv) the ambient temperature θ_a and v) the electronics temperature θ_e.
2) Sensor electrical losses are $p_s = I^2 R$ (self-heating).
3) Sensors are assumed to exchange heat with shield and environment.
4) Wires are assumed to exchange heat with sensor, environment, shields and electronics.

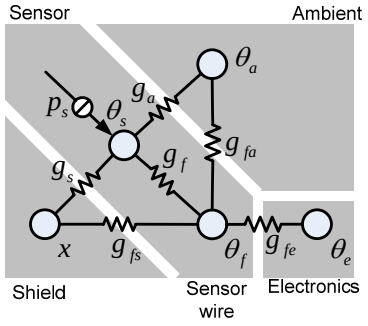

Fig. 10 Sensor heat exchange network.

Self-heating can be accurately compensated below 1 mK using two-current method [20]. Unfortunately, it demands rather long measurement periods, which are not suitable to the present real-time application. Therefore, the following analysis assumes self-heating is not compensated.

A static (low-frequency) model must be kept as conservative because of the high thermal capacitance of the cavity. Solving the network in Fig. 10, the linear relation

$$e \cong c_a(\mathbf{g})\theta_a + c_e(\mathbf{g})\theta_e + c_s(\mathbf{g})\,p_s \qquad (30)$$

is obtained, where $\mathbf{g}$ collects thermal conductances $g_f, \ldots$ in Fig. 10. Coefficients in (30) may be referred to as sensitivities. Numerical values of $\mathbf{g}$ were obtained from theoretical considerations, and from the manufacturer's data of three off-the-shelf sensors. They are: i) MINCO S35 Nickel-Iron flexible sensor (Sensor A), ii) MINCO S200PD platinum industrial sensor (Sensor B), and iii) Measurement Specialties silver leadless chip to be soldered on the shield surface (sensor C). The resulting values, in mW/K, of the different conductances in Fig. 10 are listed in Table I

TABLE I. THERMAL PARAMETERS OF THREE COMMERCIAL SENSORS

Sensor	g_s	g_f	g_a	g_{fs}	g_{fe}	g_{fa}
A	25	8.8	0.28	50	0.3	0.4
B	15	8.8	0	50	0.3	0.4
C	360	8.8	0.002	50	0.3	0.4

Table II provides, for each sensor, the sensitivities defined in (30), with respect to the ambient temperature θ_a, the electronics temperature θ_e, and sensor losses p_s.

TABLE II. MEASUREMENT ERROR SENSITIVITIES

Sensor	c_a [mK/K]	c_e [mK/K]	c_s [mK/mW]
A	9	1.6	30
B	3.5	0.6	55
C	0.2	0.15	2.6

Restricting to sensor self-heating, power losses and the corresponding error contribution $c_s(\mathbf{g})\,p_s$ in (30) are computed and shown in Table III.

TABLE III. MEASUREMENT ERROR DUE TO SELF-HEATING

Sensor	A	B	C
Power losses [mW], p_s	0.6	0.1	0.001
Error due to self-heating [mK], $c_s p_s$	18	5.5	0.003

Table III indicates sensor C is an appropriate selection to respect thermal stability requirement (16) without any special mounting. Were either sensors A or B employed, specific mounting should be designed so as to reduce self-heating in Table III (columns A and B) below millikelvin as required by (16).

B. TEC design

Thermo-electric coolers must be designed versus ambient-to-chamber thermal gradient. To this end, the same dynamics in Fig. 7 is employed, keeping x_f and x_r as the state variables, ignoring all disturbance sources other than ambient temperature, and making explicit TEC Joule losses, as they are relevant to design. State equations of the cold and hot sides are as follows

$$\begin{bmatrix} C_f \dot{x}_f \\ C_r \dot{x}_r \end{bmatrix}(t) = \begin{bmatrix} -g_T - g_{fa} & g_T \\ g_T & -g_T - g_{ra} \end{bmatrix} \begin{bmatrix} x_f \\ x_r \end{bmatrix}(t) + \\ + \begin{bmatrix} -\alpha \\ \alpha \end{bmatrix} I(t) + \begin{bmatrix} g_{fa} \\ g_{ra} \end{bmatrix} \theta_a(t) + \frac{1}{2}\begin{bmatrix} I^2(t)R \\ I^2(t)R \end{bmatrix} \qquad (31)$$

where x_f, x_r and θ_a are the cold-side, radiator and ambient temperatures, respectively, I is the TEC driving current and R is the electrical resistance. All other parameters have been defined either in Fig. 7 or in (23).

At equilibrium, (31) provides the gradient $x_f - \theta_a$ as a function of the TEC current. Solving for I and looking for a stationary point, the maximum gradient current holds

$$I_{\Delta\theta\max} = \alpha\left[2R\left(2g_T/g_{ra}+1\right)\right]^{-1}. \qquad (32)$$

It depends on the TEC parameters α, R, and g_T, and on the radiator conductance g_{ra}, but not on the cold-side-to-ambient conductance g_{fa}. Instead, the peak gradient does depend on g_{fa}, which is the design parameter. A plot of the latter as a function of g_{fa} is shown in Fig. 11, assuming $N = 4$ TEC units at room temperature, and the values $\alpha \approx 60$ V, $R \approx 4\ \Omega$, $g_{ra} = 3$ W/K.

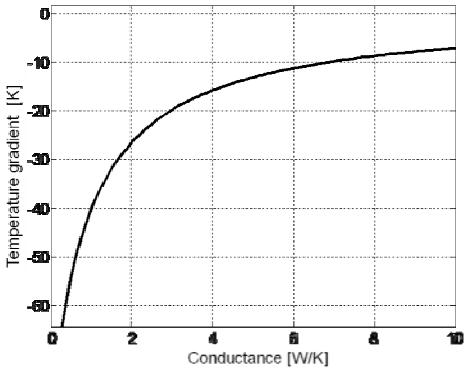

Fig. 11 Peak thermal gradient as a function of cold-side conductance.

As a design guideline, assuming the external surface of the vacuum chamber is close to 0.5 m^2, a gradient of 20 K could be obtained by insulating the chamber surface so as to guarantee $g_{fa} \le 3$ W/K.

VI. Preliminary Experimental Results

Preliminary experimental results are of two types, and univariate.

1) The first experiment concerns the preliminary cavity (Section I.B), made by ULE and in vacuum: it is thermally regulated by a heater blanket wound around the cylindrical surface of the cavity (Fig. 1). Two thermistor heads (in the form of a bin) are fastened to the cavity surface at the two extremities close to the mirror substrates (lateral sensors); the third is mounted in a central position. The thermistor heads are not perfectly insulated from vacuum chamber radiation, acting as a disturbance.
2) The second experiment, in air, concerns an aluminum plate, emulating the reference sink wall, carrying a thermal load, emulating chamber envelope and bath. The plate is thermally regulated by three TEC units connected in series. Three thermistors are inserted into the aluminum plate.

A. Preliminary cavity thermal regulation

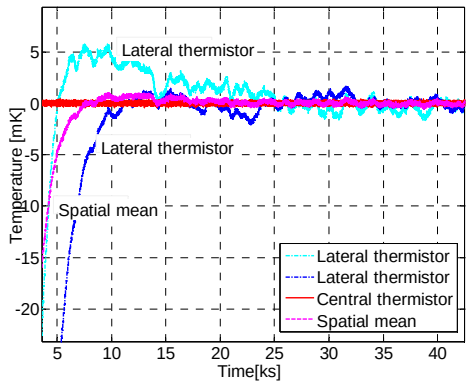

Fig. 12 Central, lateral and spatial-mean thermistor measures.

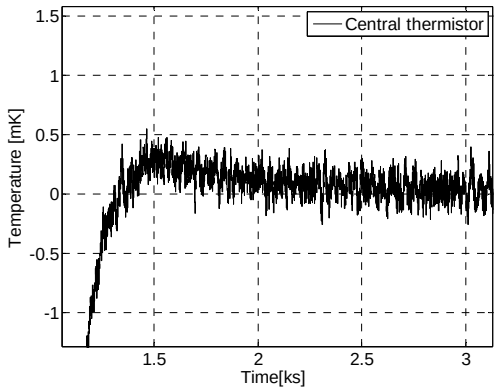

Fig. 13 Set-point acquisition by central thermistor.

Fig. 12 shows regulated (central) and lateral thermistor measurements and their spatial mean, from an overnight test lasting more than 10 hours. The central thermistor reaches the millikelvin tolerance around the set-point temperature $\underline{\theta} = 23$ °C from about 20°C in less than 30 minutes, with a low residual overshoot, only due to quantization (Fig. 13). The same occurs to lateral thermistors but, due to rather different heater-to-thermistor dynamics – thermistors are located at the heater edges - an overshoot of the order of 0.1 K occurs, being recovered in about 3 hours. Overshoot may be attenuated by slowing down reference trajectory. Fig. 12 also shows the estimated spatial mean, which is expected to be conservative with respect to the actual value, due to lateral thermistor location at the cavity extremes. The spatial mean δ_0 and the gradient δ_1 defined in Section II.B are here obtained from

$$\begin{aligned} \delta_0 &= \alpha\theta(0) + (1-\alpha)\delta_1, \ 2/3 \le \alpha \le 1 \\ \delta_1 &= \left(\theta(L) - \theta(-L)\right)/2 \end{aligned} \quad . \tag{33}$$

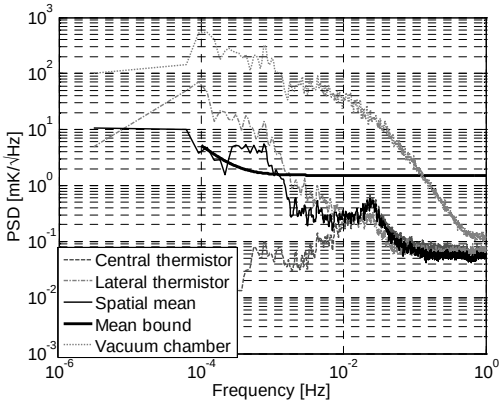

Fig. 14 Lateral and central thermistor measurements together with spatial mean and bound.

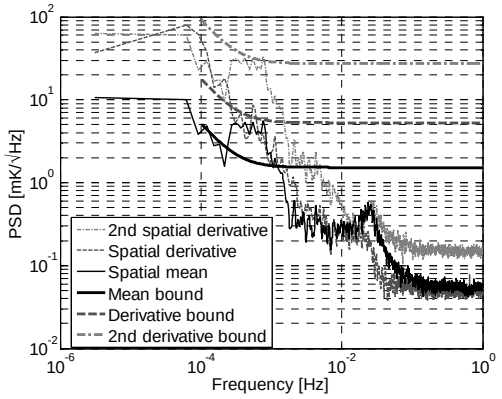

Fig. 15 Spatial mean and derivatives along the cavity.

Fig. 14 shows the PSD of the time history in Fig. 12 after set-point achievement (> 12500 s). Lateral thermistors overlap to some extent, especially at lower frequencies. The spatial mean exceeds the target bound in a limited band below 1 mHz, very likely due to laboratory conditioning, affecting differently lateral thermistors. The vacuum chamber PSD shows that (i) the thermal insulation (mainly vacuum) contributes to the central thermistor thermal stability by a factor close to 25, (ii) the closed-loop BW approaches 25 mHz. Moreover, active control contributes to

lateral thermistor stability from 25 mHz down to 2 mHz. Fig. 15 shows the estimated spatial first and second derivatives δ_1 and δ_2 together with their bounds. The gradient looks the most critical, as it shows excessive thermal asymmetry along the cavity. Fig. 15 shows experimental data to be rather close to target bounds, notwithstanding the provisional, simple and rough set-up.

Fig. 16 shows that the measured frequency instability significantly overlaps the profile of the spatial-mean PSD, except for a plateau between 0.1 and 1 mHz due to ambient conditioning, and for two peaks at 5 and 10 mHz. Unfortunately, the overlapping scale factor is much greater than the expected glass CTE, suggesting that dimensional instability is driven by other causes: the latter have been referred to clamping suspensions. Frequency instability was obtained by beating the laser source locked to the cavity with a second laser source locked to molecular absorption lines.

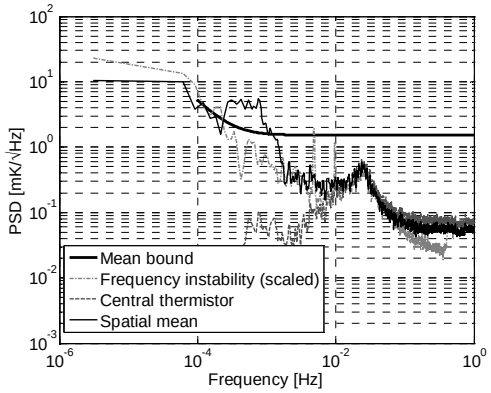

Fig. 16 Spatial mean and frequency beat (instability).

B. Plate TEC regulation

An aluminum plate carrying a thermal load, in air, is regulated by three TEC units in series (3 A max) whose hot side is placed over an aluminum sink. Their cold side supports the aluminum plate. The control causes the plate temperature to move between set-points, ranging from 10 to 40° C, without overshooting and in a reasonable time. The set-point must be maintained thereafter.

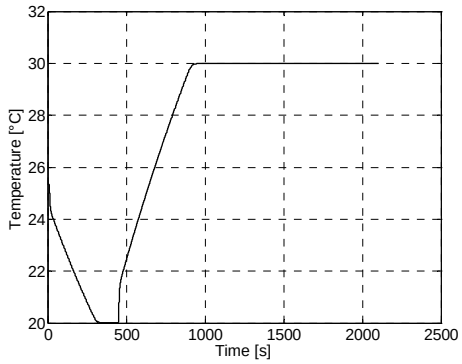

Fig. 17 Measured temperature between 20 °C and 30°C set points.

Fig. 17 shows the actual temperature profile from an initial temperature of 25 °C to 20 °C set point and then to 30 °C. The slew rate, close to 20 mK/s, is limited by TEC current (see Fig. 19), and thermal load which, after 10 s, slows down the initial slew rate imposed by TEC current and plate capacitance (notice the 2 K step before 500 s in Fig. 17).

Fig. 18 shows set-point acquisition of the central thermistor, free of overshoot. The jitter - the measured control error - standard deviation is less than 0.5 mK. Control BW is close to 30 mHz as in the preliminary cavity control (Section A). BW is mainly limited by neglected thermistor dynamics having cutoff frequency $f_s \cong 0.1$ Hz as in Section IV. Measure quantization is less than 0.5 mK.

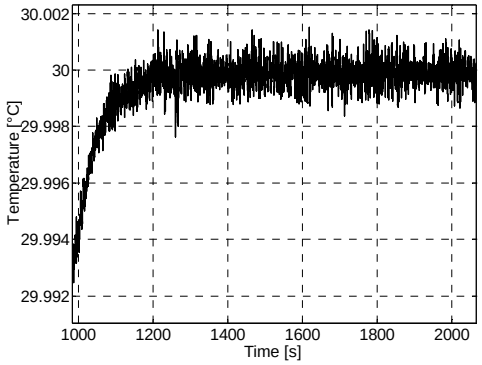

Fig. 18 Enlargement of Figure 17 at set point achievement.

Fig. 19 shows the TEC current for the temperature profile in Fig. 17: it reaches positive (cooling) and negative (heating) bounds during set-point switching. The final variable offset, less than 1 A (absolute value) is due to compensation of heat losses.

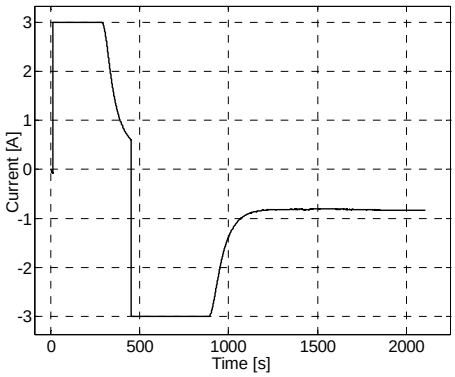

Fig. 19 TEC current.

VII. CONCLUSIONS

The multilayer active thermal control relevant to a new optical reference cavity for space applications has been outlined. Cavity design has been guided by preliminary experiments, suggesting improved suspensions to withstand launch loads, and active control concepts to exploit zero-expansion temperature of the ULE glass in a wide range of spacecraft environments. Relevant considerations for the

design of thermal sensor and actuators have been provided. The new cavity is under commissioning together with a maquette for control test and set-up.

ACKNOWLEDGMENTS

The authors are indebted to the reviewers for their helpful remarks and suggestions, to professor Elio Bava, Politecnico di Torino, and to the staff of the Regione Piemonte project "Riferimenti ultrastabili di frequenza ottica per interferometria laser in applicazioni spaziali (Ultra stable optical references for space laser interferometry)" for helpful discussions and support.

REFERENCES

[1] S. Vitale et al. "LISA and its in-flight precursor SMART-2", *Nucl. Phys. B, Proc. Suppl.*, Vol. 110, No. 2, p. 209-216, 2002.

[2] M. Ollivier et al. "Nulling interferometry for the DARWIN space mission", *Comptes Rendus de l'Académie des Sciences, Series IV, Physics*, Vol. 2, No. 1, pp. 149-156, 2001.

[3] S. Nagano et al. "Displacement measuring technique for satellite-to–satellite laser interferometer to determine Earth's gravity field", *Meas. Sci. Technol.*, Vol. 15, No. 12, pp. 2406-2411, Dec. 2004

[4] J. C. Berquist, W. M. Itano and D. J. Wineland "Laser stabilization to a single ion", in *Frontiers in Laser Spectroscopy*. Hansch T.W and Inguscio M eds. (North-Holland, Amsterdam, 1994), p. 359-376.

[5] L. Marmet et al. "Precision frequency measurement of the 2S1/2-2D5/2 transition of Sr+ with a 674-nm diode laser locked to an ultrastable cavity", *IEEE Trans. Instr. Meas.*, Vol. 46, No. 2, p. 169-172, 1997.

[6] B.C. Young, F.C. Cruz, W. M. Itano and J. C. Berquist "Visible lasers with subhertz linewidths", *Physical Rev. Letters*, Vol. 82, No. 19, p. 3799-3802, 1999.

[7] R. J. Cruz et al. "The LISA benchtop simulator at the University of Florida", *Class. Quantum Grav.*, Vol. 23, p. S751-S760, 2006.

[8] G. O. Beale and M. Li "Robust temperature control for microwave heating of ceramics", *IEEE Trans. on Industrial Electronics*, Vol. 44, No. 1, p. 124-131, February 1997.

[9] C-H. Lu and C-C. Tsai "Adaptive Predictive Control With Recurrent Neural Network for Industrial Processes: An Application to Temperature Control of a Variable-Frequency Oil-Cooling Machine" , *IEEE Trans. on Industrial Electronics*, Vol. 55, No. 3, p. 1366–1375, March 2008.

[10] C-H. Lu and C-C. Tsai "Adaptive decoupling predictive temperature control for an extrusion barrel in a plastic injection molding process", *IEEE Trans. on Industrial Electronics*, Vol. 48, No. 5, p. 968-975, October 2001.

[11] A. Tay, H. Chua, Y. Wang and Y. Ngo "Equipment Design and Control of Advanced Thermal Processing Module in Lithography", *IEEE Trans. on Industrial Electronics*, Vol. 57, No. 3, p. 1112-1119, March 2010.

[12] C-F. Juang and J-S. Chen "Water bath temperature control by a recurrent fuzzy controller and its FPGA implementation", *IEEE Trans. on Industrial Electronics*, Vol.53, No. 3, p. 941-949, June 2006.

[13] U. Has and D. Wassilew "Temperature control for food in pots on cooking hobs", *IEEE Trans. on Industrial Electronics*, Vol. 46, No. 1, p. 1030-1034, October 1999.

[14] C. Guo, Q. Song and W. Cai "A Neural Network Assisted Cascade Control System for Air Handling Unit", *IEEE Trans. on Industrial Electronics*, Vol. 54, No. 1, p. 620–628, February 2007.

[15] Y.-L. Liao, J.-H. She and M. Wu "Integrated hybrid-PSO and Fuzzy.NN decoupling control for temperature of reheating furn", *IEEE Trans. on Industrial Electronics*, Vol. 56, No. 7, p. 2704-2714, July 2009.

[16] E. Canuto "Embedded Model Control: outline of the theory", *ISA Trans.*, Vol. 46, No. 3, June 2007, p. 363-377, 2007.

[17] E. Canuto and F. Musso "Digital control of interferometric metrology lines", *European Journal of Control*, Vol. 13, No. 4, p. 398-418, 2007.

[18] E. Canuto, F. Musso and L. Massotti "Automation and control of Fabry-Pérot interferometers", *IEEE Trans. on Industrial Electronics*, Vol. 54, No. 2, p. 848-857, April 2007.

[19] E. Canuto, F. Musso and L. Massotti "Embedded Model Control: sub-micro radian horizontality of the thrust-stand Nanobalance", *IEEE Trans. on Industrial Electronics*, Vol. 55, No. 9, p. 3435-3446, September 2008.

[20] V Batagelj, J Bojkovski and J Drnovšek "Methods of reducing the uncertainty of the self-heating correction of a standard platinum resistance thermometer in temperature measurements of the highest accuracy", *Meas. Sci. Technol.*, Vol.14, p. 2151-2158, 2003.

José Ospina (M'08) was born in Santa Fé de Bogotà, Colombia. He received a degree in Electrical Engineering from Pontificia Universidad Javeriana, Bogotà, Colombia. He is currently a Ph.D. student in Information and System Engineering at Politecnico di Torino, Turin, Italy. His main interests include automation, control, modeling and data elaboration.

Enrico Canuto (SM'09) was born in Varallo (Piemonte), Italy. He received a degree in Electrical Engineering from Politecnico di Torino, Turin, Italy, where he joined the staff as Associate Professor of Automatic Control in 1983.

From 1982 to 1997 he contributed to data reduction of the European astrometric mission Hipparcos. Technological studies in view of scientific and drag-free space missions, like Gaia and GOCE provided the opportunity of applying Embedded Model Control to drag-free satellites and to electro-optics. He contributed to the conception, design and implementation of the 'Nanobalance' interferometric thrust-stand, capable of sub-micronewton accuracy. His present studies address space formation control and planetary reentry. His research interests cover all the entire field of control problems that are challenging because of complexity, uncertainty and precision.

Andrés Molano Jimenez (S'07) was born in Santa Fé de Bogotá, Colombia. In 2007 he received a degree in Electrical Engineering from Pontificia Universidad Javeriana, Bogotá, Colombia. He is currently a Ph.D. student in Information and System Engineering at the Politecnico di Torino, Turin, Italy. His main research interests include applied control, hardware design, spacecraft attitude control and drag free satellites.

Wilber Acuña-Bravo (S'09) was born in Mérida, Venezuela, in 1980. He received a degree in Electrical Engineering from Universidad del Quindío, Armenia, Colombia, and a M.S. degree in Control Engineering from Universidad de Los Andes, Mérida, Venezuela. Currently he is a Ph.D. student in Information and System Engineering at Politecnico di Torino, Turin, Italy. His research interests include mobile hydraulic control systems and control applications.